

# On-Nanowire Axial Heterojunction Design for High-Performance Photodetectors

Pengfei Guo,<sup>†,‡,§,⊥</sup> Jinyou Xu,<sup>†</sup> Ke Gong,<sup>†</sup> Xia Shen,<sup>†</sup> Yang Lu,<sup>†</sup> Yang Qiu,<sup>†</sup> Junqi Xu,<sup>†</sup> Zhijun Zou,<sup>†</sup> Chunlei Wang,<sup>†</sup> Hailong Yan,<sup>†</sup> Yongsong Luo,<sup>\*,†</sup> Anlian Pan,<sup>\*,§</sup> Han Zhang,<sup>||</sup> Johnny C. Ho,<sup>‡</sup> and Kin Man Yu<sup>\*,‡</sup>

<sup>†</sup>Key Laboratory of Advanced Micro/Nano Functional Materials, School of Physics and Electronic Engineering, Xinyang Normal University, Xinyang 464000, China

<sup>‡</sup>Department of Physics and Materials Science, City University of Hong Kong, Kowloon, Hong Kong

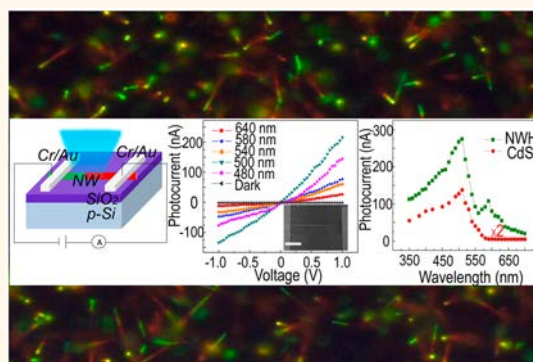
<sup>§</sup>Key Laboratory for Micro-Nano Physics and Technology of Hunan Province, State Key Laboratory of Chemo/Biosensing and Chemometrics, School of Physics and Electronics, and <sup>⊥</sup>Department of Materials Science and Engineering, Hunan University, Changsha 410082, China

<sup>||</sup>Key Laboratory of Optoelectronic Devices and Systems of Ministry of Education and Guangdong Province, Shenzhen University, Shenzhen 518060, China

## Supporting Information

**ABSTRACT:** We report the growth of high-quality CdS/CdS<sub>x</sub>Se<sub>1-x</sub> axial heterostructure nanowires (NWHs) *via* a temperature-controlled chemical vapor deposition method. Microstructural characterizations revealed that these NWHs have a single-crystalline structure with abrupt heterojunctions. Local photoluminescence and mapping near the heterojunctions show only two separated narrow band-edge emission bands from the two different adjacent semiconductors, further demonstrating the high-quality of these heterostructures. Moreover, the photodetector based on the single NWH shows a performance (higher responsivity ( $1.18 \times 10^2$  A/W), faster response speed (rise  $\sim 68$   $\mu$ s, decay  $\sim 137$   $\mu$ s), higher  $I_{\text{on}}/I_{\text{off}}$  ratio ( $10^5$ ), higher EQE ( $3.1 \times 10^4$  %), and broader detection range (350–650 nm)) at room temperature superior to that of photodetectors based on single band gap nanostructures. This work suggests a much simpler route to achieve superior NWHs for applications in optoelectronic devices.

**KEYWORDS:** nanowire, heterostructure, high performance, photodetectors



Nanowires (NWs) are of particular interest due to their promising applications in highly integrated devices and systems.<sup>1–11</sup> With a unique one-dimensional footprint and versatile physical properties, semiconductor NWs have been applied in the fields of photonics and optoelectronics.<sup>12–15</sup> In particular, heterostructure nanowires (NWHs) are the crucial building blocks for all kinds of fundamental optical elements in most semiconductor-based optoelectronic devices, such as all-optical switches,<sup>19,20</sup> light-emitting diodes,<sup>18</sup> solar cells,<sup>16,17</sup> and high-sensitivity photodetectors.<sup>21–24</sup> In light of the excellent photoconductive properties of groups II–VI NWs with laterally or axially modulated band gaps, they are potential candidates for multifunctional and/or high-performance semiconductor nanowire-based devices.<sup>25,26</sup> So far, a large number of photodetectors have been investigated based on nanostructures with different natural band gaps.<sup>27–33</sup> However, it is still very challenging to achieve a broad spectral response photodetector made of single-composition semiconductor

NWs due to the constraints of optoelectronic transfer efficiency and light absorption ability.<sup>34,35</sup> Therefore, the synthesis of high-quality axial semiconductor NWHs *via* a controllable chemical vapor deposition (CVD) strategy to eventually realize multifunctional detectors is fundamentally important in the field of advanced materials and nanotechnology.

Compared to one-dimensional nanostructures with homogeneous composition, NWHs are expected to have a higher photon sensitivity and broader spectral response. This can be attributed to their expanded absorption band and potential-enhanced light–matter interactions at their special active junction regions.<sup>36–39</sup> In the present work, we report the growth of high-quality axial NWHs using an improved CVD

Received: May 25, 2016

Accepted: July 15, 2016

Published: July 15, 2016

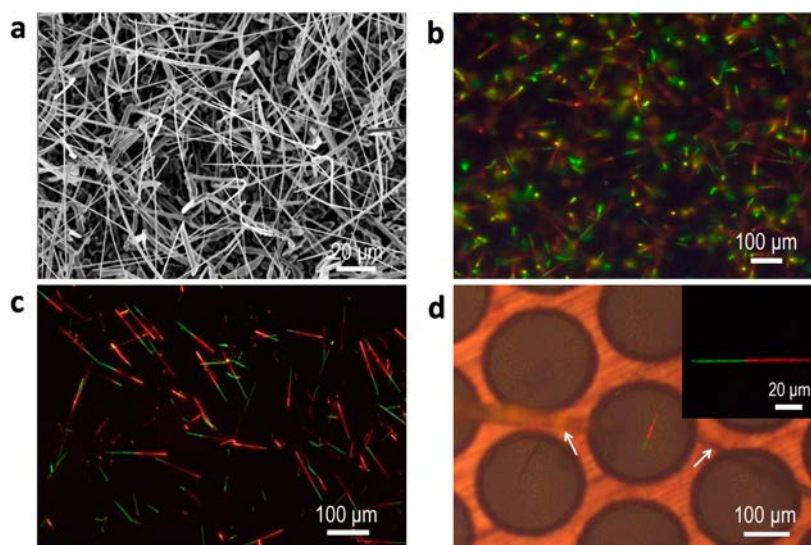


Figure 1. (a) SEM image of single-junction CdS/CdSSe NWHs. (b) Top-view photograph of the as-grown wires under a diffused 450 nm laser illumination. (c) Real-color photograph of the NWHs randomly dispersed onto a transparent  $\text{MgF}_2$  wafer under the diffused laser illumination. (d) Optical photograph of a CdS/CdSSe NWH on a copper grid, which was transferred from the grown substrate by 3D mechanical arms with two fiber probes (white arrows in d). Inset: Real-color image of the selected wire.

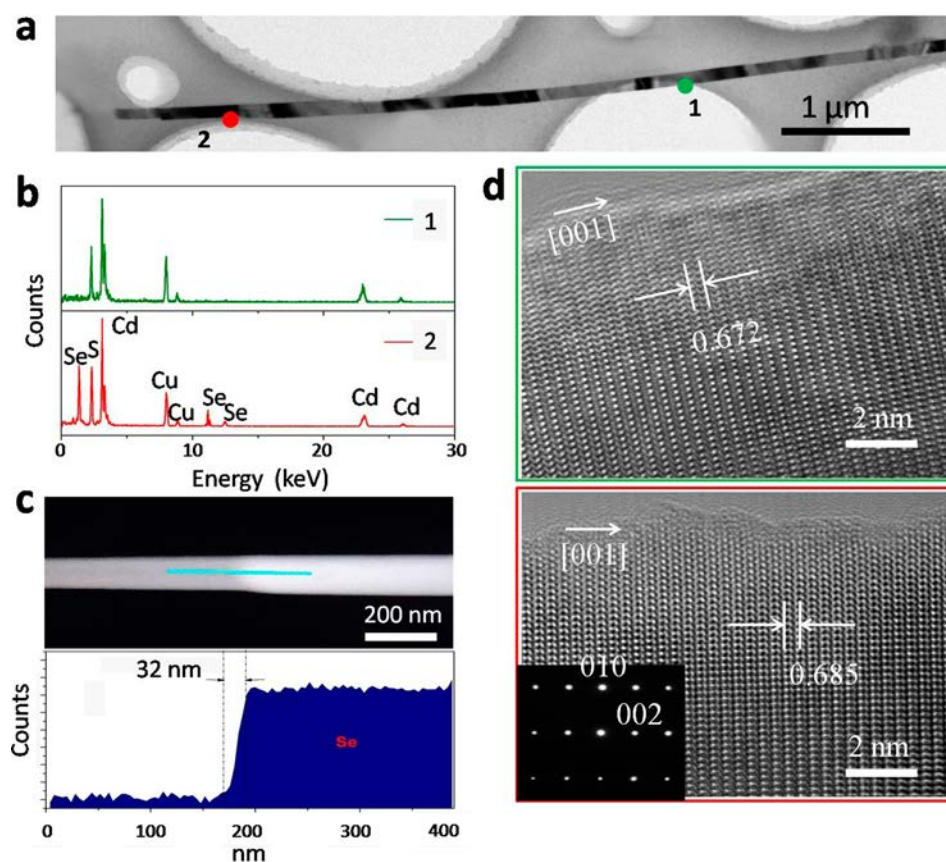
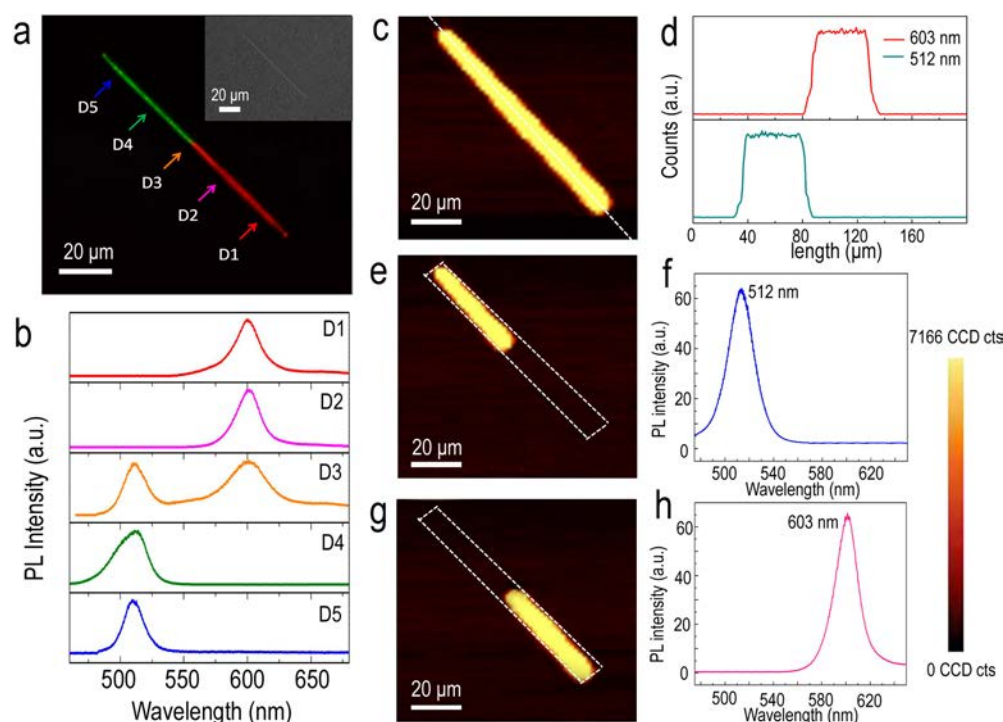


Figure 2. (a) TEM image of a single-junction CdS/CdSSe NWH (scale bar,  $1\ \mu\text{m}$ ). (b) EDX profiles of two typical positions (1 and 2) along the wire, as indicated in a. (c) HAADF STEM image of a single NWH and the element line scanning profile along the wire (cyan line). (d) HRTEM images taken from two representative positions (red and green spots in a) along the wire. Inset: Corresponding *in situ* selected area electron diffraction patterns.

strategy with a moving source. This method is capable of large-scale synthesis that can break the poor controllability of the solid evaporation sources under high temperature. Micro-structural characterization shows that these NWHs are high-

quality single crystals with abrupt interfaces. Micro-photo-luminescence ( $\mu\text{-PL}$ ) exhibits two separated narrow emission bands along the length of the heterostructures. On the basis of the unique axial nanostructures, photodetectors were con-



**Figure 3.** Room temperature optical characterization of a representative NWH. (a) Real-color photograph of a representative single-junction CdS/CdSSe NWH, which was selected on a MgF<sub>2</sub> substrate for optical characterization. Inset: Optical image of the wire. (b) Series of typical  $\mu$ -PL spectra (D1–D5) obtained from the top end to the bottom end along the axial direction, as mentioned in a. (c,d) PL mapping result and the corresponding line scanning profile results of a single-junction NWH along the wire length (as indicated by the dotted line). (e,g) Two-dimensional PL mapping and (f,h) corresponding PL spectral results during the test ranges of 508–513 and 598–603 nm, respectively.

structed. As expected, these detectors show high performance, such as a wide spectral response range of 350–650 nm, a responsivity of  $1.18 \times 10^2$  A/W, a fast response speed ( $\sim 68$   $\mu$ s), a high  $I_{\text{on}}/I_{\text{off}}$  ratio of  $10^5$ , and a high external quantum efficiency of  $3.1 \times 10^4\%$ . These characteristics are superior to the performance of regular detectors made of semiconductor nanostructures with single composition. To the best of our knowledge, this is the first report on the synthesis of single-crystalline axial CdS/CdSSe NWHs *via* CVD for visible-light photodetectors. The results imply that these high-performance photodetectors are prospective candidates for applications in photonics and optoelectronics.

## RESULTS AND DISCUSSION

Scanning electron microscopy (SEM) observation reveals that the wires have a length of several tens of micrometers with diameters ranging from 80 to 450 nm (Figure 1a). The catalyst is observed at the tip of each NW (Figure S1, Supporting Information), which reveals that these NWs were grown through the vapor–liquid–solid mechanism.<sup>37,40</sup> Meanwhile, atomic force microscopy (AFM) observation and a close-up SEM image of typical CdS/CdSSe NWHs indicate that the surfaces of the wires are very smooth (Figures S2 and S3, Supporting Information), making it a good candidate for the transmission of guided light. Figure 1b shows the top view of the real-color photograph of as-grown NWs on the original substrate under the radiation of a continuous wave (CW) 450 nm laser. There are obvious green emissions on the top of these wires. Some red emissions are also observed when the focal plane is randomly located on the bottom section of some wires. Figure 1c shows the real-color photograph of several randomly dispersed wires on a MgF<sub>2</sub> slide that were randomly removed

from the original growth substrate. As can be seen, most of the longer NWs have red and green emission, with an abrupt interface between them, indicating a high yield of NWHs by our method. In order to check the microstructural information on these NWHs, a single NW was transferred to a copper grid by home-built 3D mechanical arms with two fiber probes (see Figure S4 for the detailed transfer process, Supporting Information). Figure 1d shows the optical photograph of the transferred CdS/CdSSe NWH. The real-color image (inset) clearly displays a well-defined heterostructure interface, with red emission in one segment and green emission in the other segment.

Microstructural investigations of these NWHs were performed by transmission electron microscopy (TEM). Figure 2a shows a typical TEM image of a representative single-junction CdS/CdSSe NW heterostructure with a diameter of  $\sim 90$  nm. Energy-dispersive X-ray (EDX) spectra (Figure 2b) collected from two representative positions along the length direction of the wire (dots 1–2 in Figure 2a) reveal that position “1” mainly consists of the elements S and Cd with negligible Se, whereas position “2” is composed of considerable amounts of Se, S, and Cd. Figure 2c shows the high-angle annular dark-field (HAADF) STEM image and elemental line scanning results of a single NWH along the length direction. Abrupt increase in the Se concentration is observed at the interface (cyan line in Figure 2c). These elemental analyses, combined with the elemental line scanning profiles, reveal that these wires are actually heterostructures with CdS in one segment and CdSSe alloy in the other segment. This is also consistent with the different emissions observed under a diffused 450 nm laser illumination in real-color photographs, as shown in Figure 1. Figure 2d exhibits the high-resolution TEM



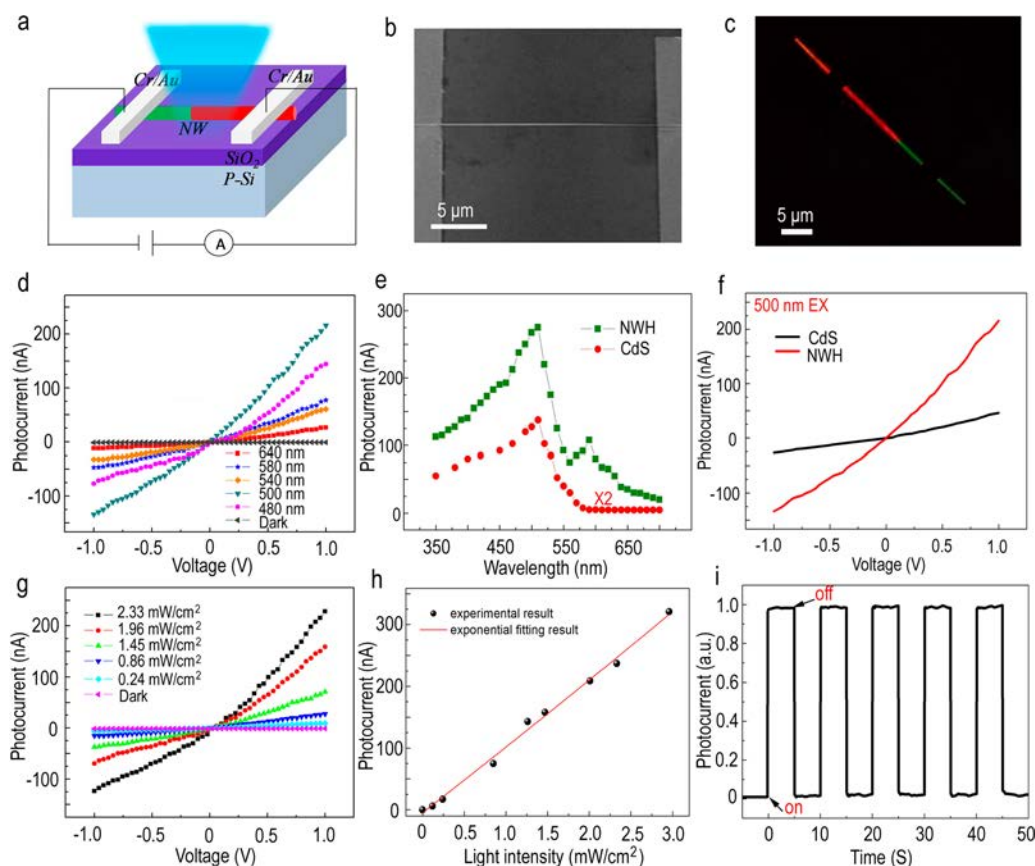


**Figure 4.** Electrical characterization of a CdS/CdSSe NWH device. (a) Schematic of a NWH-based photodetector. (b,c) SEM image and real-color image of the same NWH device under 450 nm CW laser illumination. (d)  $I$ - $V$  measurements with the illumination of different wavelengths ( $2.33 \text{ mW/cm}^2$ ) or in dark. (e,f) Wavelength-dependent photocurrent response of CdS/CdSSe NWH-based and pure CdS NW-based photodetectors. (g)  $I$ - $V$  measurements under 500 nm laser illumination with various power densities. (h) Photocurrent of the NWH photodetector as a function of illumination power density with 500 nm photons under 1 V bias. (i) NWH device's on-off response upon 500 nm light illumination at a voltage of 3 V ( $2.86 \text{ mW/cm}^2$ ).

(HRTEM) images derived from typical positions of the wire (see the green and red cycles in Figure 2a), where a high-quality single-crystalline nanostructure without significant defects is clearly observed. The measured lattice parameter  $c$  in the CdS region is 0.672 nm, consisting of the (0002) lattice spacing of wurtzite CdS; however, the lattice parameter of 0.685 nm in the other segment is slightly larger than that of the CdS segment, consistent with the (0002) lattice spacing of wurtzite  $\text{CdS}_{0.49}\text{Se}_{0.51}$  ( $x \approx 0.49$ ).<sup>4</sup> These results explicitly clarify that we have realized the synthesis of high-quality axial CdS/CdSSe NWHs.

The optical properties of these axial CdS/CdSSe NWHs were investigated by spatially resolved  $\mu$ -PL spectra along the length of the wire with a confocal  $\mu$ -PL system. Figure 3a shows a typical real-color image of a NWH with a length of  $\sim 80 \mu\text{m}$  and a diameter of  $\sim 90 \text{ nm}$  under a diffused CW 450 nm laser illumination. The inset shows the corresponding optical image of the same NWH. A list of  $\mu$ -PL spectra were obtained from five representative positions along the wire (highlighted by number "D1" to "D5" in Figure 3a), and the results are shown in Figure 3b. The PL results show that both positions "D1" and "D2" exhibit strong single-peak emissions at a wavelength of 512 nm, while positions "D4" and "D5" show emission peaks at 603 nm, corresponding to the near-band-edge emissions of CdS and  $\text{CdS}_{0.49}\text{Se}_{0.51}$  alloy, respectively. This is consistent with the HAADF STEM and HRTEM results shown in Figure 2. When

measurement was made at position D3, where we expect the CdS/CdSSe heterointerface is located, two emission peaks at 512 and 603 nm are observed. These peaks can be attributed to the emissions from the CdS and  $\text{CdS}_{0.49}\text{Se}_{0.51}$  alloy at the heterojunction region. It is worth noting that no obvious trap/defect-state-related emissions were identified across the entire wire, nor at the heterointerface region in Figure 3b, suggesting that these NWHs are high-quality NWHs with no observable optically active defects. This is in good agreement with the TEM observation in Figure 2.

Two-dimensional  $\mu$ -PL mapping along the length (dotted line) of the NWH and the corresponding PL line scanning profiles for the 512 and 603 nm emissions are shown in Figure 3c,d, respectively. It is clearly shown that the two emission bands are located at the two separated regions of the wire. The individual emission band (green, 510–515 nm; red, 601–606 nm) of  $\mu$ -PL mapping and their corresponding PL spectra shown in Figure 3e–h clearly show that the top and the bottom of the NWH correspond to the CdS (green) and  $\text{CdS}_{0.49}\text{Se}_{0.51}$  segment (red), respectively. Thus, spatially resolved  $\mu$ -PL is consistent with the structural characterization results (Figure 2), providing a direct proof that axial NWHs with two different semiconductor alloys with a sharp interface were achieved using a temperature-controlled multistep CVD method.

Figure 4a shows the schematic diagram of the photodetector that we fabricated by using an individual CdS/CdSSe NWH. In

brief, a NWH was first selected and transferred to a p-type Si substrate covered with a 200 nm thick SiO<sub>2</sub> layer, followed by laying down two separated Cr/Au (20 nm/40 nm) electrodes on the two ends of the wire. Figure 4b,c shows the SEM image and dark-field image of an individual NWH-based photodetector, respectively. A photodetector based on a single CdS NW with similar size (length = 52  $\mu$ m; diameter = 90 nm) as the NWH was also constructed and investigated for comparison, as shown in Figure S5 (Supporting Information). The current–voltage (*I*–*V*) characteristics of the NWH photodetector exposed to light of different wavelengths (2.33 mW/cm<sup>2</sup>; 640, 580, 540, 500, and 480 nm) or under dark conditions are shown in Figure 4d. It is clearly seen that the conductance of the NWH is very small in the dark condition (only  $\sim 10^{-12}$  A), while a high current of  $\sim 235$  nA is recorded at an applied voltage of 1 V when the device is illuminated with 500 nm visible light at a power intensity of 2.33 mW/cm<sup>2</sup>. Under illumination with different wavelengths (power intensity = 2.33 mW/cm<sup>2</sup>), photocurrents increase dramatically, demonstrating high sensitivity of the NWH photodetector.

Moreover, the NWH-based photodetector also exhibits a good wavelength-selective sensitivity. Figure 4e shows a comparison of the detailed wavelength-dependent photocurrent response of the CdS/CdSSe NWH-based and pure CdS NW-based photodetectors at an applied voltage of 1 V when the devices are illuminated with light of various wavelengths at the same power intensity of 2.33 mW/cm<sup>2</sup>. The results show two response bands with peak positions at 512 and 603 nm for the NWH-based device. In contrast, the CdS single-component device has only one spectral response band at 512 nm (Figure 4e) with much lower photocurrent. Because of the unique band structure of the NWH, the NWH-based device shows a wide light response range from 350 to 650 nm, which is much broader than the CdS NW device ( $\sim 350$ – $550$  nm). Figure 4f shows photocurrents of both devices under 500 nm light illumination with a power density of 2.33 mW/cm<sup>2</sup>. Under 1 V bias, the photocurrent response of the NWH photodetector (red line) is about 4 times higher than that of the single-component CdS-based device (black line).

The power density dependence photoresponse of the NWH photodetector under a 500 nm visible light illumination is shown in Figure 4g. We observed that the photocurrent of the NWH photodetector gradually increases with the rise in the light density and reaches values  $>10^{-7}$  A at a power density of 2.33 mW/cm<sup>2</sup>. Compared with the dark current ( $10^{-12}$  A), the photocurrent increases by more than 5 orders of magnitude. These results suggest that the NWH photodetector has very high sensitivity. Figure 4h shows a sublinear relationship for the light-intensity-dependent photocurrent for the device under 1 V bias. The corresponding calibration curve is also plotted in Figure 4h, and the exponential fitting result can be expressed with the equation  $y = 5.143 \times \exp(x/48.8) - 5.148$  [ $\mu$ A] and a correlation coefficient of 0.99. The external quantum efficiency (EQE), which is the number of electron–hole pairs produced by one absorbed photons,<sup>10</sup> is a critical parameter and can be expressed as

$$\text{EQE} = hcR_{\lambda}/e\lambda$$

in which  $R_{\lambda} = \Delta I/(PS)$  is the photodetector responsivity,  $\Delta I$  is the difference between the photocurrent and dark current,  $P = 2.33$  mW/cm<sup>2</sup> is the incident light power density irradiated on the wires,  $S$  is the area of wire, and  $\lambda = 500$  nm is the wavelength of irradiated light. Thereby, the obtained  $R_{\lambda}$  value

for the NWH-based device is  $1.18 \times 10^2$  A/W, and the corresponding EQE is  $3.1 \times 10^4\%$ . These measured values for the NWH device are much higher than those for the CdS NW-based photodetector we fabricated (29.5 A/W;  $7.3 \times 10^3\%$ ) as well as pure CdS NW photodetectors reported in the literature.<sup>41–43</sup> The time response of a CdS/CdSSe NWH photodetector is shown in Figure 4i, which is investigated by periodic turning on or off a 500 nm laser with the device under 1 V bias. The results exhibit a very good stability and reproducibility with rise and decay times of about 68 and 137  $\mu$ s, respectively, which are much faster than the pure CdS NW device (1.6 and 3.7 ms, Figure S5c in the Supporting Information) and the reported results for single band gap NW detectors.<sup>41–44</sup>

In light of the above results, the performance in sensitivity and response time of these NWH-based detectors are much better than pure CdS NW-based devices. These excellent properties are mainly attributed to the intermediately radiative reabsorption process in the heterostructures, which is quite different from the single band gap semiconductor device, in addition to the high-quality crystal and good Ohmic contacts. Schematics of the CdS NW-based device and its energy-band diagram in the dark and under illumination are shown in Figure 5a–c. In a CdS NW device, photogenerated carriers may either

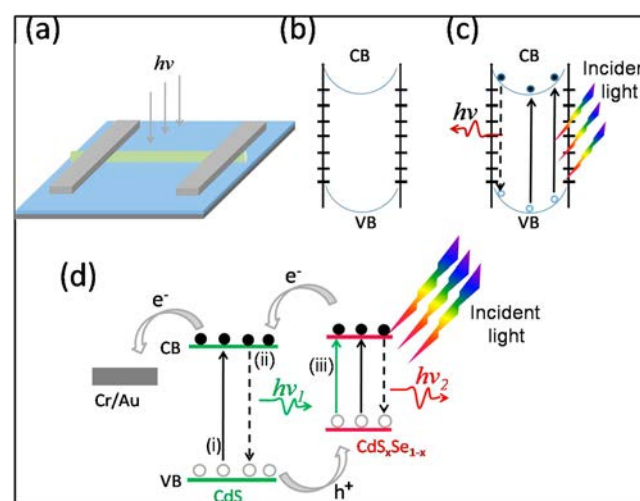


**Figure 5.** (a) Schematic of the CdS NW-based device. (b,c) Schematic illustration of the energy-band diagrams of a CdS NW in dark (b) and under light illumination (c). (d) Photoexcitation processes and energy-transfer processes for the single-junction CdS/CdSSe axial NWHs under illumination. While the incident light falls on the device, the photogenerated carriers from band to band transitions were shown in process (i). The electron–hole pairs recombined radiatively, resulting in emitted luminescence (process (ii)), and the emitted photon could be reabsorbed by the CdSSe with narrower band gap (iii). The energy-transfer process (iii) is realized from the wide band gap CdS to the narrow band gap CdSSe alloy.

drift to the contacts under an external electric field, producing photocurrent, or electron–hole pairs may recombine radiatively, emitting photons with energy close to the band gap energy of CdS. This radiative electron–hole pair recombination is one of the causes for a low photodetecting efficiency of the detector. However, there are mainly two processes: the photoexcitation process and energy-transfer process in the CdS/CdSSe NWH-based photodetector (Figure 5d). The

observed higher photocurrent is produced not only from the excitation of incident light with energy higher than that for CdS but also from the excited photons with energy lower than the band gap of CdS but higher than that of  $\text{CdS}_{0.49}\text{Se}_{0.51}$ . Moreover, the radiated photons from the CdS, whose energy is higher than that of  $\text{CdS}_{0.49}\text{Se}_{0.51}$ , can be largely reabsorbed by the  $\text{CdS}_{0.49}\text{Se}_{0.51}$  and produce additional photocarriers through the transmission along the wire (Figure 5d). This reabsorption process plays the key role in the higher photocurrent and responsivity of the NWH detector. All of the above effects result in the greatly enhanced photoresponse, higher EQE value, and broader detection range of the NWH devices over that of the single band gap NW-based detectors.

## CONCLUSION

In summary, we presented the first example of high-quality CdS/CdSSe NWHs with abrupt heterojunctions by a simply modified CVD route. Next, high-performance photodetectors were successfully fabricated on the basis of these NWHs. Compared with the photodetectors from a single semiconductor NW, the heterostructure photodetector showed a higher responsivity ( $1.18 \times 10^2$  A/W), faster response speed (rise  $\sim 68$   $\mu\text{s}$ , decay  $\sim 137$   $\mu\text{s}$ ), higher  $I_{\text{on}}/I_{\text{off}}$  ratio ( $10^5$ ), higher EQE ( $3.1 \times 10^4$  %), and broader detection range (350–650 nm). These photodetectors may have potential applications in solar cells and optoelectronic systems.

## METHODS

**Material Preparation.** The NWHs were grown *via* a temperature-controlled multistep CVD strategy. The setup is based on a horizontal furnace with a 2 in. quartz tube (inner diameter = 50 mm, length = 180 cm), as schematically shown in Figure S6 (Supporting Information). In a typical growth of single-junction CdS/CdSSe NWHs, CdS and CdSe powder sources (Alfa Aesar, 99.999%) were placed in the center and at the upstream of the heating zone, respectively, and another boat with CdS powder was seated far enough away from the evaporation region before the start. A step motor attached with the quartz rods was used to push these alumina boats into or out of the evaporation region during the preparation process. A series of silicon wafers, coated with 4 nm thick gold films, were located at the depositional area for the collection of the product. A nitrogen gas flow was introduced into the chamber at a fast rate (120 sccm, 60 min) to purge the oxygen from the chamber before heating up the furnace. The temperature in the center of the furnace was then increased to 780 °C at a rate of 28 °C  $\text{min}^{-1}$  to start the growth. After the growth of CdSSe NWs at 260 mbar, the furnace temperature was decreased to 580 °C at a rate of 25 °C  $\text{min}^{-1}$ . The furnace temperature of 580 °C was kept for another 30 min, which defined the isolation time, to enable the former source vapor (CdS and CdSe) to be totally evacuated before the next growth step. At the end of the isolation time, the CdS boat outside the heating zone was then pushed into the heating zone to replace the former CdSe and CdS boats at a rate of 8 cm  $\text{min}^{-1}$  by the step motor. Then the furnace temperature was increased to 830 °C into the final growth stage and maintained for 40 min. Lastly, the furnace was naturally cooled to room temperature.

**Optical Characterization.** The  $\mu\text{-PL}$  measurement was performed by a confocal optical system. The excitation laser beam (450 nm output) was focused (spot size,  $\sim 5$   $\mu\text{m}$ ) by a microscope objective (Nikon,  $\times 20$ ) and then pumped locally at the NWHs. The far-field optical image was recorded by a charge-coupled device color camera. Local excitation and detection were used in this  $\mu\text{-PL}$  measurement.

**Device Fabrication and Measurements.** The CdS/CdSSe NWHs and CdS NWs were transferred to cleaned Si/SiO<sub>2</sub> substrates (350 nm) by two fiber probes, as shown in Figure S4 (Supporting Information), followed by spin-coating with MMA and PMMA. Electron-beam lithography (JEOL 6510 with NPGS) was then

employed to define the source and drain patterns. Cr/Au (20 nm/40 nm) was employed as S/D ohmic electrodes on NW photodetectors. Device measurements of CdS/CdSSe NWHs and pure CdS NW photodetectors were performed on the probe station with a Keithley 4200 semiconductor parameter analyzer.

## ASSOCIATED CONTENT

### Supporting Information

The Supporting Information is available free of charge on the ACS Publications website at DOI: 10.1021/acsnano.6b03458.

Experimental setup details; SEM image of a single NW; section analysis of the AFM images of typical CdS/CdSSe NWHs; transfer process of a single wire from the original substrate to the copper grid; electrical characterization of a CdS NWH device for comparison (PDF)

## AUTHOR INFORMATION

### Corresponding Authors

\*E-mail: ysluo@xyynu.edu.cn.

\*E-mail: anlian.pan@hnu.edu.cn.

\*E-mail: kinmanyu@cityu.edu.hk.

### Notes

The authors declare no competing financial interest.

## ACKNOWLEDGMENTS

The authors thank Professor Qiaoliang Bao (Monash University) for helpful discussions, and Dr. Chaoping Liu (City University of Hong Kong) for spectral characterization of nanowires. This work was financially supported by the Hong Kong Scholars Program (No. XJ2015013), Nan Hu Young Scholar Supporting Program of XYNU, Scientific Research Program of XYNU (No. 15003), Major Preresearch Program of XYNU (No. 2015-ZDYY-176), National Natural Science Foundation of China (Nos. 61574122, 51502257, and 61504116), Key research program in the University of Henan Province (No. 17A140028), and Innovative Research Team (in Science and Technology) in the University of Henan Province (No. 13IRTSTHN018).

## REFERENCES

- (1) Agarwal, R.; Barrelet, C. J.; Lieber, C. M. Lasing in Single Cadmium Sulfide Nanowire Optical Cavities. *Nano Lett.* **2005**, *5*, 917–923.
- (2) Yan, R. X.; Park, J. H.; Choi, Y.; Heo, C. J.; Yang, S. M.; Lee, L. P.; Yang, P. D. Nanowire-based Single-Cell Endoscopy. *Nat. Nanotechnol.* **2012**, *7*, 191–196.
- (3) Guo, P. F.; Zhuang, X. J.; Xu, J. Y.; Zhang, Q. L.; Hu, W.; Zhu, X. L.; Wang, X. X.; Wan, Q.; He, P. B.; Zhou, H.; et al. Low-Threshold Nanowire Laser Based on Composition-Symmetric Semiconductor Nanowires. *Nano Lett.* **2013**, *13*, 1251–1256.
- (4) Ma, R. M.; Dai, L.; Huo, H. B.; Xu, W. J.; Qin, G. G. High-Performance Logic Circuits Constructed on Single CdS Nanowires. *Nano Lett.* **2007**, *7*, 3300–3304.
- (5) Liu, X.; Gu, L. L.; Zhang, Q. P.; Wu, J. Y.; Long, Y. Z.; Fan, Z. Y. All-Printable Band-Edge Modulated ZnO Nanowire Photodetectors with Ultra-High Detectivity. *Nat. Commun.* **2014**, *5*, 4007.
- (6) Cheng, C. W.; Liu, B.; Yang, H. Y.; Zhou, W. W.; Sun, L.; Chen, R.; Yu, S. F.; Zhang, J. X.; Gong, H.; Sun, H. D.; Fan, H. J. Hierarchical Assembly of ZnO Nanostructures on SnO<sub>2</sub> Backbone Nanowires: Low-Temperature Hydrothermal Preparation and Optical Properties. *ACS Nano* **2009**, *3*, 3069–3076.
- (7) Zheng, Z.; Gan, L.; Li, H. Q.; Ma, Y.; Bando, Y.; Golberg, D.; Zhai, T. Y. A Fully Transparent and Flexible Ultraviolet-Visible



Photodetector Based on Controlled Electrospun ZnO-CdO Heterojunction Nanofiber Arrays. *Adv. Funct. Mater.* **2015**, *25*, 5885–5894.

(8) Shen, G. Z.; Chen, D.; Chen, P. C.; Zhou, C. W. Vapor-Solid Growth of One-Dimensional Layer-Structured Gallium Sulfide Nanostructures. *ACS Nano* **2009**, *3*, 1115–1120.

(9) Xia, Y. N.; Yang, P. D.; Sun, Y. G.; Wu, Y. Y.; Mayers, B.; Gates, B.; Yin, Y. D.; Kim, F.; Yan, H. Q. One-Dimensional Nanostructures: Synthesis, Characterization, and Applications. *Adv. Mater.* **2003**, *15*, 353–389.

(10) Li, L.; Wu, P. C.; Fang, X. S.; Zhai, T. Y.; Dai, L.; Liao, M. Y.; Koide, Y.; Wang, H. Q.; Bando, Y.; Golberg, D. Single-Crystalline CdS Nanobelts for Excellent Field-Emitters and Ultrahigh Quantum-Efficiency Photodetectors. *Adv. Mater.* **2010**, *22*, 3161–3165.

(11) Long, Y. Z.; Yu, M.; Sun, B.; Gu, C. Z.; Fan, Z. Y. Recent Advances in Large-Scale Assembly of Semiconducting Inorganic Nanowires and Nanofibers for Electronics, Sensors and Photovoltaics. *Chem. Soc. Rev.* **2012**, *41*, 4560–4580.

(12) Zhai, T. Y.; Fang, X. S.; Bando, Y.; Dierre, B.; Liu, B. D.; Zeng, H. B.; Xu, X. J.; Huang, Y.; Yuan, X. L.; Sekiguchi, T.; Golberg, D. Characterization, Cathodoluminescence, and Field-Emission Properties of Morphology-Tunable CdS Micro/Nanostructures. *Adv. Funct. Mater.* **2009**, *19*, 2423–2430.

(13) Xu, J. Y.; Zhuang, X. J.; Guo, P. F.; Zhang, Q. L.; Huang, W. Q.; Wan, Q.; Hu, W.; Wang, X. X.; Zhu, X. L.; Fan, C. Z.; et al. Wavelength-Converted/Selective Waveguiding Based on Composition-Graded Semiconductor Nanowires. *Nano Lett.* **2012**, *12*, 5003–5007.

(14) Pan, J.; Utama, M. I. B.; Zhang, Q.; Liu, X. F.; Peng, B.; Wong, L. M.; Sum, T. C.; Wang, S. J.; Xiong, Q. H. Composition-Tunable Vertically Aligned  $\text{CdS}_x\text{Se}_{1-x}$  Nanowire Arrays via van der Waals Epitaxy: Investigation of Optical Properties and Photocatalytic Behavior. *Adv. Mater.* **2012**, *24*, 4151–4156.

(15) Guo, Y. B.; Zhang, Y. J.; Liu, H. B.; Lai, S. W.; Li, Y. L.; Li, Y. J.; Hu, W. P.; Wang, S.; Che, C. M.; Zhu, D. B. Assembled Organic/Inorganic p–n Junction Interface and Photovoltaic Cell on a Single Nanowire. *J. Phys. Chem. Lett.* **2010**, *1*, 327–330.

(16) Zhang, C.; Yan, Y.; Yao, J. N.; Zhao, Y. S. Manipulation of Light Flows in Organic Color-Graded Microstructures towards Integrated Photonic Heterojunction Devices. *Adv. Mater.* **2013**, *25*, 2854–2859.

(17) Zhai, T. Y.; Li, L.; Ma, Y.; Liao, M. Y.; Wang, X.; Fang, X. S.; Yao, J. N.; Bando, Y.; Golberg, D. One-Dimensional Inorganic Nanostructures: Synthesis, Field-Emission and Photodetection. *Chem. Soc. Rev.* **2011**, *40*, 2986–3004.

(18) Piccione, B.; Cho, C. H.; van Vugt, L. K.; Agarwal, R. All-Optical Active Switching in Individual Semiconductor Nanowires. *Nat. Nanotechnol.* **2012**, *7*, 640–645.

(19) Li, L.; Lu, H.; Yang, Z. Y.; Tong, L. M.; Bando, Y.; Golberg, D. Bandgap-Graded  $\text{CdS}_x\text{Se}_{1-x}$  Nanowires for High-Performance Field-Effect Transistors and Solar Cells. *Adv. Mater.* **2013**, *25*, 1109–1113.

(20) Pan, C. F.; Dong, L.; Zhu, G.; Niu, S.; Yu, R.; Yang, Q.; Liu, Y.; Wang, Z. L. High-Resolution Electroluminescent Imaging of Pressure Distribution Using a Piezoelectric Nanowire LED Array. *Nat. Photonics* **2013**, *7*, 752–758.

(21) Rai, S. C.; Wang, K.; Ding, Y.; Marmon, J. K.; Bhatt, M.; Zhang, Y.; Zhou, W. L.; Wang, Z. L. Piezo-Phototronic Effect Enhanced UV/Visible Photodetector Based on Fully Wide Band Gap Type-II ZnO/ZnS Core/Shell Nanowire Array. *ACS Nano* **2015**, *9*, 6419–6427.

(22) Lin, H. W.; Liu, H. B.; Qian, X. M.; Lai, S. W.; Li, Y. J.; Chen, N.; Ouyang, C.; Che, C. M.; Li, Y. L. Constructing a Blue Light Photodetector on Inorganic/Organic p–n Heterojunction Nanowire Arrays. *Inorg. Chem.* **2011**, *50*, 7749–7753.

(23) Wang, X. F.; Song, W. F.; Liu, B.; Chen, G.; Chen, D.; Zhou, C. W.; Shen, G. Z. High-Performance Organic-Inorganic Hybrid Photodetectors Based on P3HT: CdSe Nanowire Heterojunctions on Rigid and Flexible Substrates. *Adv. Funct. Mater.* **2013**, *23*, 1202–1209.

(24) Xiang, J.; Lu, W.; Hu, Y. J.; Wu, Y.; Yan, H.; Lieber, C. M. Ge/Si Nanowire Heterostructures as High-Performance Field-Effect Transistors. *Nature* **2006**, *441*, 489–493.

(25) Xu, J. Y.; Ma, L.; Guo, P. F.; Zhuang, X. J.; Zhu, X. L.; Hu, W.; Duan, X. F.; Pan, A. L. Room-Temperature Dual-Wavelength Lasing from Single-Nanoribbon Lateral Heterostructures. *J. Am. Chem. Soc.* **2012**, *134*, 12394–12397.

(26) Jiang, Y.; Zhang, W. J.; Jie, J. S.; Meng, X. M.; Fan, X.; Lee, S. T. Photoresponse Properties of CdSe Single-Nanoribbon Photodetectors. *Adv. Funct. Mater.* **2007**, *17*, 1795–1800.

(27) Jie, J. S.; Zhang, W. J.; Jiang, Y.; Meng, X. M.; Li, Y. Q.; Lee, S. T. Photoconductive Characteristics of Single-Crystal CdS Nanoribbons. *Nano Lett.* **2006**, *6*, 1887–1892.

(28) Fang, X. S.; Bando, Y.; Liao, M. Y.; Zhai, T. Y.; Gautam, U. K.; Li, L.; Koide, Y.; Golberg, D. An Efficient Way to Assemble ZnS Nanobelts as Ultraviolet-Light Sensors with Enhanced Photocurrent and Stability. *Adv. Funct. Mater.* **2010**, *20*, 500–508.

(29) Li, Q. H.; Gao, T.; Wang, T. H. Optoelectronic Characteristics of Single CdS Nanobelts. *Appl. Phys. Lett.* **2005**, *86*, 193109.

(30) Kung, S. C.; van der Veer, W. E.; Yang, F.; Donovan, K. C.; Penner, R. M. 20  $\mu\text{s}$  Photocurrent Response from Lithographically Patterned Nanocrystalline Cadmium Selenide Nanowires. *Nano Lett.* **2010**, *10*, 1481–1485.

(31) Zhai, T. Y.; Fang, X. S.; Liao, M. Y.; Xu, X. J.; Li, L.; Liu, B. D.; Koide, Y.; Ma, Y.; Yao, J. N.; Bando, Y.; Golberg, D. Fabrication of High-Quality  $\text{In}_2\text{Se}_3$  Nanowire Arrays toward High-Performance Visible-Light Photodetectors. *ACS Nano* **2010**, *4*, 1596–1602.

(32) Zhai, T. Y.; Li, L.; Wang, X.; Fang, X. S.; Bando, Y.; Golberg, D. Recent Developments in One-Dimensional Inorganic Nanostructures for Photodetectors. *Adv. Funct. Mater.* **2010**, *20*, 4233–4248.

(33) Deng, K.; Li, L. CdS Nanoscale Photodetectors. *Adv. Mater.* **2014**, *26*, 2619–2635.

(34) Liu, H.; Sun, Q.; Xing, J.; Zheng, Z. Y.; Zhang, Z. L.; Lü, Z. Q.; Zhao, K. Fast and Enhanced Broadband Photoresponse of a ZnO Nanowire Array/Reduced Graphene Oxide Film Hybrid Photodetector from the Visible to the Near-Infrared Range. *ACS Appl. Mater. Interfaces* **2015**, *7*, 6645–6651.

(35) Miao, J. S.; Hu, W. D.; Guo, N.; Lu, Z. Y.; Zou, X. M.; Liao, L.; Shi, S. X.; Chen, P. P.; Fan, Z. Y.; Ho, J. C.; Li, T. X.; Chen, X. S.; Lu, W. Single InAs Nanowire Room-Temperature Near-Infrared Photodetectors. *ACS Nano* **2014**, *8*, 3628–3635.

(36) Hu, L. F.; Yan, J.; Liao, M. Y.; Xiang, H. J.; Gong, X. G.; Zhang, L. D.; Fang, X. S. An Optimized Ultraviolet-A Light Photodetector with Wide-Range Photoresponse Based on ZnS/ZnO Biaxial Nanobelt. *Adv. Mater.* **2012**, *24*, 2305–2309.

(37) Guo, P. F.; Hu, W.; Zhang, Q. L.; Zhuang, X. J.; Zhu, X. L.; Zhou, H.; Shan, Z. P.; Xu, J. Y.; Pan, A. L. Semiconductor Alloy Nanoribbon Lateral Heterostructures for High-Performance Photodetectors. *Adv. Mater.* **2014**, *26*, 2844–2849.

(38) Wang, K.; Chen, J. J.; Zhou, W. L.; Zhang, Y.; Yan, Y. F.; Pern, J.; Mascarenhas, A. Direct Growth of Highly Mismatched Type II ZnO/ZnSe Core/Shell Nanowire Arrays on Transparent Conducting Oxide Substrates for Solar Cell Applications. *Adv. Mater.* **2008**, *20*, 3248–3253.

(39) Hu, L. F.; Yan, J.; Kim, Y.; Fei, G. T.; Watanabe, K.; Sekiguchi, T.; Zhang, L.; Fang, X. S. Cathodoluminescence and Photoconductive Characteristics of Single-Crystal Ternary CdS/CdSe/CdS Biaxial Nanobelts. *Small* **2015**, *11*, 1531–1536.

(40) Pan, A. L.; Liu, R. B.; Sun, M. H.; Ning, C. Z. Quaternary Alloy Semiconductor Nanobelts with Bandgap Spanning the Entire Visible Spectrum. *J. Am. Chem. Soc.* **2009**, *131*, 9502–9503.

(41) Li, Q. H.; Penner, R. M. Photoconductive Cadmium Sulfide Hemicylindrical Shell Nanowire Ensembles. *Nano Lett.* **2005**, *5*, 1720–1725.

(42) Wei, T. Y.; Huang, C. Y.; Hansen, B. J.; Lin, Y. F.; Chen, L. J.; Lu, S. Y.; Wang, Z. L. Large Enhancement in Photon Detection Sensitivity via Schottky-Gated CdS Nanowire Nanosensors. *Appl. Phys. Lett.* **2010**, *96*, 013508.

(43) Li, L.; Yang, S. M.; Zhang, X. T.; Wang, L. J.; Jiang, Z. D.; Lin, Q. J.; Wang, C. Y.; Han, F.; Peng, N. C. Single CdS Nanowire Photodetector Fabricated by FIB. *Microelectron. Eng.* **2014**, *126*, 27–30.

(44) Pena, D. J.; Mbindyo, J. K. N.; Carado, A. J.; Mallouk, T. E.; Keating, C. D.; Razavi, B.; Mayer, T. S. Template Growth of Photoconductive Metal-CdSe-Metal Nanowires. *J. Phys. Chem. B* **2002**, *106*, 7458.